

Exploring masses and CNO surface abundances of red giant stars

Ghina M. Halabi^{1*}, Mounib El Eid¹

¹*Department of Physics, American University of Beirut, Bliss Street 11-0236, Beirut 1107 2020, Lebanon*

Accepted: May 2015. Received ; in original form

ABSTRACT

A grid of evolutionary sequences of stars in the mass range $1.2\text{--}7M_{\odot}$, with solar-like initial composition is presented. We focus on this mass range in order to estimate the masses and calculate the CNO surface abundances of a sample of observed red giants. The stellar models are calculated from the zero-age main sequence till the early asymptotic giant branch (AGB) phase. Stars of $M \leq 2.2M_{\odot}$ are evolved through the core helium flash. In this work, an approach is adopted that improves the mass determination of an observed sample of 21 RGB and early AGB stars. This approach is based on comparing the observationally derived effective temperatures and absolute magnitudes with the calculated values based on our evolutionary tracks in the Hertzsprung-Russell diagram. A more reliable determination of the stellar masses is achieved by using evolutionary tracks extended to the range of observation. In addition, the predicted CNO surface abundances are compared to the observationally inferred values in order to show how far standard evolutionary calculation can be used to interpret available observations and to illustrate the role of convective mixing. We find that extra mixing beyond the convective boundary determined by the Schwarzschild criterion is needed to explain the observational oxygen isotopic ratios in low mass stars. The effect of recent determinations of proton capture reactions and their uncertainties on the $^{16}\text{O}/^{17}\text{O}$ and $^{14}\text{N}/^{15}\text{N}$ ratios is also shown. It is found that the $^{14}\text{N}(p, \gamma)^{15}\text{O}$ reaction is important for predicting the $^{14}\text{N}/^{15}\text{N}$ ratio in red giants.

Key words: convection, nuclear reactions, nucleosynthesis, abundances - stars: evolution - stars: low-mass

1 INTRODUCTION

After the main sequence evolutionary phase, stars evolve to the red giant branch (RGB). This evolution is initiated by the ignition of shell H-burning surrounding the He core, whose energy flux causes the envelope to expand and the star evolves to the RGB. The expansion increases the opacity and leads to the development of a deep convective envelope. This is the first dredge up event (FDUP), as convection mixes up the products of H-burning to the surface altering the surface composition of the star.

In the mass range $(4\text{--}7)M_{\odot}$, stars exhibit blue loops at the beginning of core He burning (see Halabi, El Eid & Champagne (2012), and references therein). The main phase of core He-burning is completed before the track evolves back to the RGB. This leads again to the deepening of envelope convection. For solar metallicity stars of $M \gtrsim 4M_{\odot}$, a second dredge up (SDUP)

can reach deeper regions, which leads to further changes in the surface abundances.

This work uses observations obtained for a sample of red giants by Tsuji (2008), hereafter Tsuji08, in order to achieve two goals: (a) to estimate the masses of these giants by matching their observationally derived effective temperatures and bolometric magnitudes to the values obtained from the evolutionary tracks in the HR diagram. This is possible since the stars are not pulsating Mira variables (see Section 3.1 for details). We are able to improve the mass determination done by Tsuji08 by using more extended evolutionary tracks to avoid the extrapolation that he partially relied on to determine the mass of some giants, (b) to compare the calculated CNO abundances of these models to those inferred from observations in the light of recent determinations of key reaction rates.

A large body of observational data is available for the surface CNO abundances in RGB stars (Lambert & Reis 1981; Harris & Lambert 1984a,b; Harris et al. 1988; Lambert et al. 1986; Gilroy & Brown 1991; Tsuji 1991;

* E-mail: gm29@aub.edu.lb

Charbonnel 1994; Tsuji 2008; Tautvaišienė et al. 2010; Piau et al. 2011). These data provide a powerful tool to get insight into the internal structure of evolved stars. In particular, comparing the predicted oxygen surface abundances to the observed data is useful to improve the treatment of convective mixing in the stellar interiors (see Section 3.2.2). Our results suggest the need for extra mixing below the edge of the convective envelope as determined by the Schwarzschild criterion in order to achieve a better agreement with observations. This extra mixing has been suggested in several investigations in connection with the evolution of field giants (Charbonnel & Do Nascimento 1998; Gratton et al. 2000), open clusters (Luck 1994; Tautvaišienė et al. 2000, 2005), globular clusters (Shetrone 2003; Pilachowski et al. 2003; Recio-Blanco & de Laverny 2007; Denissenkov et al. 2015) as well as to explain isotopic ratios in pre-solar grains (Palmerini et al. 2011, 2013; Busso et al. 2014). The abundance profile of ^{17}O of particular interest. This is because this isotope is produced by the ON-cycle which requires higher temperatures than the CN-cycle. Therefore, the ^{17}O profile exhibits a steep gradient within the central region of the star, at the position of maximum convective penetration (shown later in Fig. 4). This renders the ^{17}O surface abundance sensitive to the depth of convective mixing, stellar mass and to the nuclear reaction rates involved in the CNO cycle (El Eid 1994). We show in Section 3.2.2 how the $^{16}\text{O}/^{17}\text{O}$ ratio is useful to constrain this extra mixing. The low surface carbon isotopic ratios in low mass stars however, can not be explained by our extra-mixing treatment. Other non-standard mixing mechanisms may need to be invoked as shown in Section 3.2. Ramstedt & Olofsson (2014) also discuss carbon isotopic ratios in AGB stars in connection with their recent estimations of circumstellar $^{12}\text{CO}/^{13}\text{CO}$ abundance ratios based on radiative transfer analysis of radio line emission observations.

Concerning the nuclear reaction network, there has been extensive experimental work recently on updated determinations of major reaction rates, including those of the CNO cycle. One set of rates that we use (Sergi et al. 2014) was obtained with the Trojan Horse method (La Cognata et al. 2010), which is an indirect technique that is able to provide more reliable reaction rate cross-sections at low temperatures where measurements in the astrophysical energy range are available. Other sets, obtained by Sallaska et al. (2013) and Iliadis et al. (2010) are evaluated based on Monte Carlo techniques (Longland et al. 2010). This method provides a median rate which -under certain conditions- resembles the commonly referred to “recommended” rate, as well as a low rate and a high rate which, unlike the “upper” and “lower” limits of classical rates, have a well-defined statistical meaning. The effect of these recent determinations of the proton capture reactions including the $^{14}\text{N}(\text{p}, \gamma)^{15}\text{O}$ rate on the isotopic ratios $^{16}\text{O}/^{17}\text{O}$ and $^{14}\text{N}/^{15}\text{N}$ is investigated.

This paper is organized as follows. Section 2 describes the calculations and provides a summary of the observational data used in this work. The results are presented in Section 3. Mass determinations and comparison with previous works are provided in Section 3.1. In Section 3.2, we describe the surface abundance profiles and the effects of extra mixing. The effect of nuclear reaction rates is discussed in Section 3.3. Concluding remarks are given in Section 4.

2 MODEL CALCULATIONS

The evolutionary sequences presented in this work are obtained using the stellar evolution code HYADES as described in El Eid et al. (2009), with the recent modifications outlined in Halabi, El Eid & Champagne (2012). This code is a one-dimensional implicit Lagrangian code based on a hydrodynamical method which solves the stellar structure equations on an adaptive grid. Mass-loss is included using semi-empirical rates adjusted to the global parameters of the star. The rates are used according to a Mira pulsation period (P) (Vassiliadis & Wood 1992). For $P < 100$ d, Reimers (1975) mass-loss rate is used, with $\eta = 1$. For $100 \leq P < 500$ d we use a more effective rate according to Bowen (1988). For $P \geq 500$ d, the superwind mass-loss rate during the AGB is used as suggested by Vassiliadis & Wood (1992).

2.1 Analyzing the overshooting region

In the context of the Mixing Length Theory (MLT), the extension of a convective zone is determined by the Schwarzschild criterion, that is when $\nabla_{\text{rad}} > \nabla_{\text{ad}}$, where ∇_{rad} and ∇_{ad} are the radiative and adiabatic temperature gradients, respectively.

Within this framework, a long-standing issue is to fix the boundary of the convective zone. In the local description of the MLT, mixing beyond the Schwarzschild boundary is introduced in a parameterized way. According the multi-dimensional hydrodynamic simulations by Freytag et al. (1996), a local description of an extra mixing (or overshooting) may be introduced in terms of an exponentially decaying diffusion coefficient:

$$D(z) = D_o e^{-\frac{2z}{H_p}} \quad (1)$$

where $z = |r_{\text{boundary}} - r|$ is the overshoot distance, D_o is the diffusion coefficient at the boundary of the convective envelope obtained from the Mixing Length Theory (see Langer et al. (1985)), H_p is the pressure scale height and f is a free parameter which is a measure of the efficiency of this extra partial mixing. It is clear from Eq. 1 that for smaller values of f , D has a steeper profile, or equivalently less extra mixing. As f increases, this extra mixing extends further beyond the formal convective boundary. The numerical simulations by Freytag et al. (1996) find $f = 0.25 \pm 0.05$ and 1.0 ± 0.1 for A-stars and DA white dwarfs, respectively. We will use the observationally inferred oxygen isotopic ratio in red giants to constrain the value of f (see Section 3.2).

The mixing of chemical elements is achieved by solving the diffusion equation given by:

$$\frac{dX_i}{dt} = \frac{\partial}{\partial M_r} [(4\pi r^2 \rho)^2 D \frac{\partial X_i}{\partial M_r}] \quad (2)$$

where r is the radius, ρ is the mass density and D is the diffusion coefficient given by Eq. 1 when used in the overshoot region, otherwise it is equal to D_o in a convective zone according to the Schwarzschild criterion.

To illustrate the effect of the treatment of mixing described above, Fig. 1 shows the behavior of ∇_{rad} , ∇_{ad} as well as the profiles of the diffusion coefficient and hydrogen (X_{H}) as a function of interior mass. This is done for a $1.2M_{\odot}$ model during the first dredge up phase (FDUP) after the star has evolved to the red giant branch.

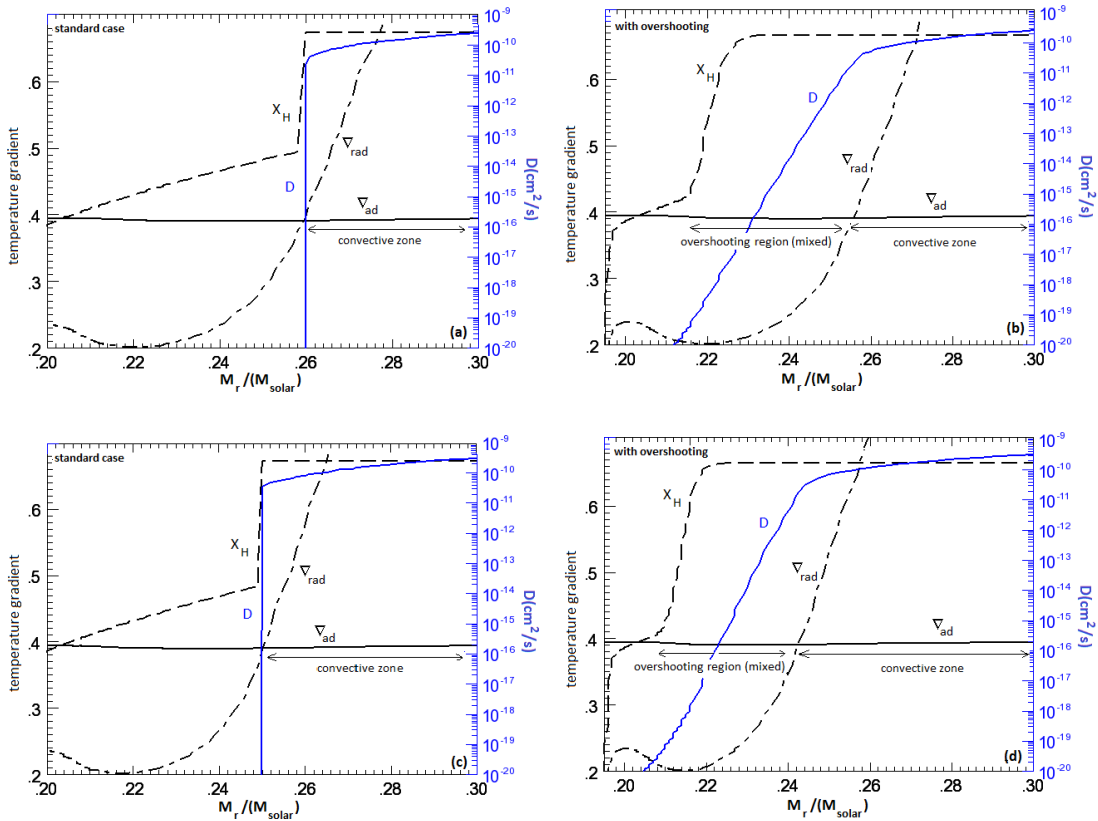


Figure 1. Physical quantities related to the condition of convection at the bottom of the convective envelope in a $1.2M_{\odot}$ star during FDUP, for (a) the standard stellar model and (b) the model with overshooting using $f=0.125$. (c) and (d) are the same as (a) and (b), respectively, but 3×10^5 years later. ∇_{rad} and ∇_{ad} are the radiative and adiabatic temperature gradients, respectively. Also shown are the hydrogen profile (left scale) and diffusion coefficient profile (right scale).

The left-hand panel of Fig. 1 shows the extension of the convective envelope in the standard models, i.e. without overshooting where the abrupt drop of the diffusion coefficient D is visible along with the vertical drop of X_{H} . The right panel shows the behavior with overshooting. It is seen that in the latter case, mixing is extended into the radiative region where $\nabla_{\text{rad}} < \nabla_{\text{ad}}$. The lower panels show the profiles at the next time-step, 3×10^5 years later. In both cases, the convective envelope deepens in mass as FDUP proceeds, but it is deeper in the case with overshooting, where the change in composition alters the opacity so that $\nabla_{\text{rad}} > \nabla_{\text{ad}}$ becomes satisfied deeper in mass. Therefore, overshooting does not only induce extra mixing but also drives convective instability. Details of the present calculations with this overshooting or extra diffusive mixing are provided in Section 3.2.2.

2.2 Observational data

A sample of red giant stars has been observed by Tsuji08 as given in Table 1. The effective temperatures were obtained using the infrared flux method (Blackwell et al. 1980), while the absolute bolometric magnitudes were determined from the bolometric luminosities obtained by integrating the spectral energy distributions and the Hipparcos parallaxes. The uncertainty on the effective temperature is estimated to be

100K, and the error on the bolometric magnitude is mainly due to the error on the parallaxes. In the next section, the effective temperatures and bolometric magnitudes are used to determine the stellar masses of the observed giants using our evolutionary tracks, which cover the whole range of observations.

3 EVOLUTIONARY RESULTS

Evolutionary sequences of stars in the mass range $(1.2-7.3)M_{\odot}$ are calculated from the zero-age main sequence till the early AGB phase. Stars of $M \geq 3M_{\odot}$ exhibit blue loops starting at the onset of central helium burning, which become more extended for stars of mass $\gtrsim 4M_{\odot}$. A detailed discussion on this evolutionary phase has been presented in Halabi, El Eid & Champagne (2012). Stars of masses $\leq 2.2M_{\odot}$ and solar-like initial composition evolve through the core He-flash (Kippenhahn & Weigert 1990; Mocák et al. 2010; Bildsten et al. 2012). We find that for $M < 2M_{\odot}$, the helium flash starts off-center owing to the cooling via the plasma and photo neutrino energy losses. In the mass range $2 \leq M/M_{\odot} \leq 2.2$ the helium flash starts at the center since these stars evolve at relatively lower central densities so the cooling by neutrino energy losses is less efficient.

The core helium flash requires very short time steps to

Table 1. Spectral type, effective temperatures and bolometric magnitudes (Tsuji08).

Object(BS/HD)	Spectral type	T_{eff} (K)	M_{bol} (mag)
δ Vir (4910)	M3III	3643	-2.4 ± 0.3
α Tau (1457)	K5+III	3874	-1.7 ± 0.2
RRUMi (5589)	M4.5III	3397	-3.4 ± 0.3
RZ Ari (687)	M6III	3341	-3.5 ± 0.6
δ Oph (6056)	M0.5III	3790	-2.2 ± 0.3
ν Vir (4517)	M1III	3812	-2.2 ± 0.4
τ^4 Eri (1003)	M3+IIIa	3712	-2.9 ± 0.4
10 Dra (5226)	M3.5III	3730	-2.9 ± 0.3
β Peg (8775)	M2.5II-III	3606	-3.3 ± 0.2
30g Her (6146)	M6-III	3298	-4.2 ± 0.4
σ Lib (5603)	M2.5III	3596	-3.4 ± 0.5
R Lyr (7157)	M5III	3313	-4.3 ± 0.3
μ Gem (2286)	M3III	3643	-3.3 ± 0.3
OP Her (6702)	M5II	3325	-4.4 ± 0.8
ρ Per (921)	M4II	3523	-4.1 ± 0.4
α Cet (911)	M1.5IIIa	3909	-3.2 ± 0.3
λ Aqr (8698)	M2.5III	3852	-3.4 ± 0.7
XY Lyr (7009)	M5II	3300	-5.1 ± 1.1
δ^2 Lyr (7139)	M4II	3420	-5.5 ± 0.8
α Her (6406)	M5Ib-II	3293	-5.8 ± 1.6
BS6861(6861)	M4	3600	-5.2 ± 2.0

accommodate the rapidly changing variables. In our calculation, the time step is of the order of less than a year during the core helium flash. For stars of masses in excess of $2.2M_{\odot}$, no significant degeneracy effects occur and core He-burning proceeds under hydrostatic conditions.

3.1 Mass evaluation

In the work by Tsuji08, the masses of the red giant stars listed in Table 1 are derived using the evolutionary tracks by Claret (2004). A main difference between our code and that of Claret (2004) is that the latter used Caughlan & Fowler (1988) rates for the basic nuclear reactions in the network, while our used reaction rates are updated according to the JINA REACLIB database (Cyburt et al. 2010). This is expected to introduce modifications on the evolutionary tracks. Another difference is that Claret assumes core overshooting, with an overshooting distance of $0.2H_p$ for the whole mass range and ignores envelope overshooting. Core overshooting results in a bigger core mass and affects the evolutionary tracks and the stellar lifetimes. In the sample considered here, most of the stars are low-mass stars which have very small or no convective core at all, thus applying the same amount of overshooting at the convective

core boundary would result in a large amount of mixing that yields results which are inconsistent with observations (Woo & Demarque 2001). In order to avoid this artifact, core overshooting is not included in our calculation.

Moreover, the tracks by Claret (2004) are not extended enough, so that extrapolations were needed at temperatures below 3200K during the RGB phase for about half of the stars in the sample studied by Tsuji08. In this calculation, the stars are evolved until the early AGB phase without relying on extrapolation. Moreover, mass-loss is included, and we report the masses of the evolved stars rather than their initial masses, which improves the mass determination, particularly for the higher masses where mass-loss becomes more effective.

Adopting the values of M_{bol} and T_{eff} given in Table 1, the evolutionary tracks shown in Fig. 2 are used to evaluate the stellar masses. It is important to note here that a direct comparison of the theoretical temperature to that inferred observationally wouldn't have been possible if the stars are pulsating Mira variables, in which case a radius cannot be strictly defined and any comparison wouldn't hold. Even the term effective temperature may become questionable for the very evolved AGB stars featuring strong pulsations and mass loss rates (Baschek et al. 1991; Lebzelter et al. 2010). However, in this sample, the stars are on the RGB or early AGB phase, and thus, haven't yet experienced any thermal pulsations. This allows a reliable comparison between the predicted effective temperatures and the observationally inferred ones. The theoretical bolometric magnitude is obtained using the well known relation: $M_{bol} = 4.75 - 2.5 \log(L/L_{\odot})$.

As seen in Fig. 3, our evolutionary tracks describe well the advanced evolutionary stage of these stars. Having obtained the mass of every star using these tracks, it is possible to identify its evolutionary stage and compare its CNO surface abundances with the observational data. This will be described in Section 3.2.

The stellar masses are given in Table 2. For completeness, masses obtained by other works for some stars are included (Maillard 1974; Smith & Lambert 1985; Harris et al. 1988; Decin et al. 1997). The error on the mass is determined from the error bars on the observational M_{bol} and T_{eff} . Table 2 shows that our values are systematically lower than those by Tsuji08. We attribute this mainly to two reasons:

(a) The stars are evolved to the stage where they are observed, that is, we do not use any extrapolated tracks as done in Tsuji08.

(b) Mass-loss is taken into consideration, which becomes significant for the more massive stars.

Moreover, it is clear from Table 2 that our errors on the masses are also lower. Calculating the tracks up to advanced stages helps to get better evaluation of the masses of red giants.

3.2 CNO Surface Abundances in Red Giants

3.2.1 Predictions of surface abundances with standard mixing

This section presents the results for the surface CNO abundances of the studied sample of stars. These are then com-

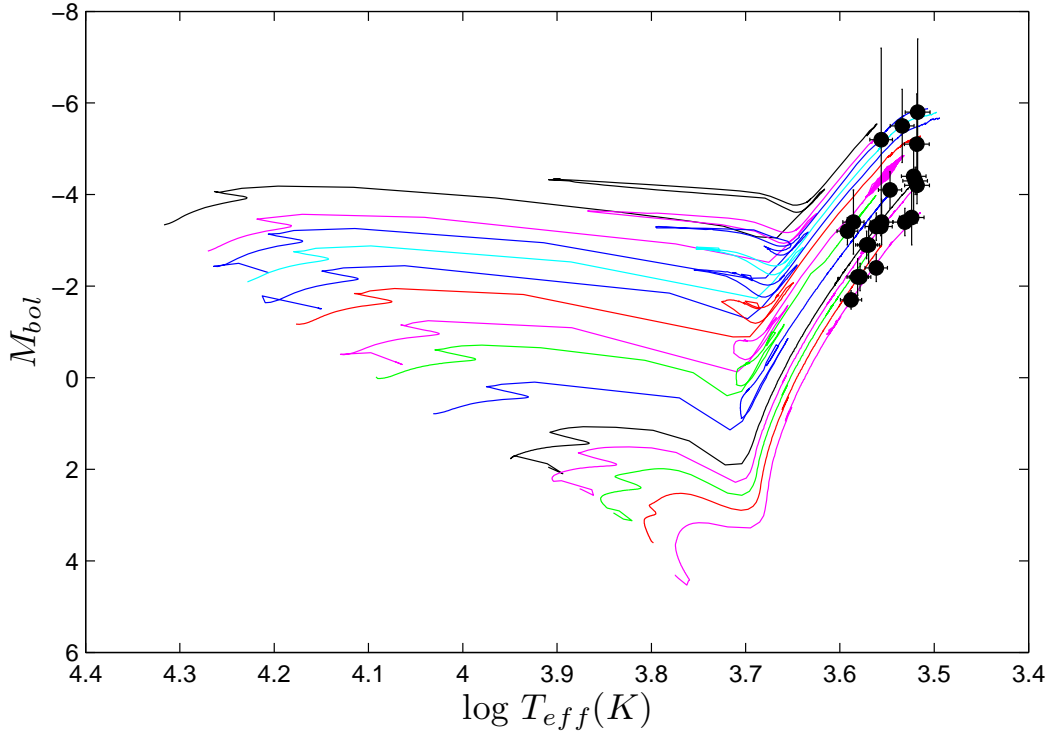


Figure 2. Bolometric magnitude (M_{bol}) versus effective temperature (T_{eff}) showing the present evolutionary tracks of stars of masses $(1.2-7)M_{\odot}$. Also shown is the observed sample listed in Table 1.

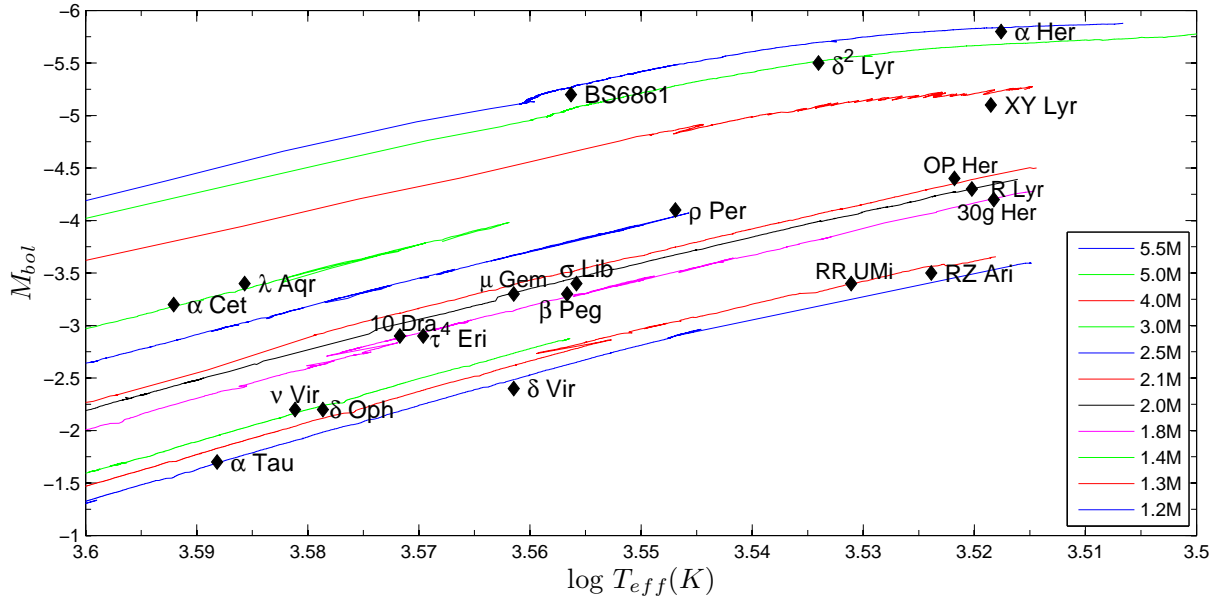


Figure 3. The evolutionary tracks together with the observed red giants listed in Table 1. Note that the observed data points have errors as indicated in Table 1.

Table 2. *a*: present work (M_{RGB} is the mass on the RGB, including mass-loss), *b*: Tsuji08, *c*: Smith and Lambert (1985), *d*: Harris et al. (1988), *e*: Decin et al. (1997), *f*: El Eid (1994). The masses are given in solar units. Note that the error on the mass by Tsuji08 increases for more massive stars, which may be related to the inaccuracy in the parallax measurements.

Object(BS/HD)	$M_{initial}^a$	M_{RGB}^a	M^b	$M(\text{others})$
δ Vir (4910)	1.2 ± 0.2	1.19 ± 0.2	1.4 ± 0.3	2.0^c
α Tau (1457)	1.2 ± 0.2	1.20 ± 0.2	1.5 ± 0.3	$1.5^{c,d}$
RRUMi (5589)	1.3 ± 0.1	1.15 ± 0.1	1.6 ± 0.3	
RZ Ari (687)	1.3 ± 0.2	1.14 ± 0.2	1.5 ± 0.4	
δ Oph (6056)	1.4 ± 0.2	1.39 ± 0.2	1.6 ± 0.3	
ν Vir (4517)	1.4 ± 0.4	1.39 ± 0.4	1.7 ± 0.4	2.0^c
τ^4 Eri (1003)	1.8 ± 0.3	1.73 ± 0.3	2.0 ± 0.4	
10 Dra (5226)	1.8 ± 0.3	1.74 ± 0.3	2.1 ± 1.8	
β Peg (8775)	1.8 ± 0.3	1.70 ± 0.3	2.2 ± 0.3	$1.7^{c,d,e,f}$
30g Her (6146)	1.8 ± 0.3	1.65 ± 0.3	2.0 ± 0.6	4.0^c
σ Lib (5603)	2.0 ± 0.2	1.90 ± 0.2	2.2 ± 0.5	
R Lyr (7157)	2.0 ± 0.2	1.80 ± 0.2	2.1 ± 0.5	
μ Gem (2286)	2.0 ± 0.5	1.90 ± 0.5	2.3 ± 0.5	$2.0^{d,f}$
OP Her (6702)	2.1 ± 0.4	1.90 ± 0.4	2.3 ± 1.0	
ρ Per (921)	2.5 ± 0.4	2.40 ± 0.5	3.2 ± 0.5	
α Cet (911)	3.0 ± 0.5	2.96 ± 0.5	3.6 ± 0.4	
λ Aqr (8698)	3.0 ± 0.5	2.96 ± 0.5	3.7 ± 1.2	
XY Lyr (7009)	4.0 ± 1.0	3.0 ± 1.0	3.7 ± 1.5	
δ^2 Lyr (7139)	5.0 ± 1.0	4.5 ± 1.0	5.5 ± 2.0	
α Her (6406)	5.5 ± 1.5	4.0 ± 1.0	5.0 ± 2.0	7.0^f
BS 6861(6861)	5.5 ± 1.5	5.35 ± 1.5	6.3 ± 4.0	

pared to the CNO isotopic ratios inferred from observations. The abundance profiles of the CNO isotopes and those of H and He prior to the FDUP are shown in Fig. 4. In order to study the variation of these abundance profiles as a function of the initial stellar mass, two sample stellar masses are shown: $1.4M_{\odot}$ (Fig. 4a) and $5M_{\odot}$ (Fig. 4b). Several features can be identified in these figures:

(a) The isotope ^{13}C is produced near the middle of the star by the CN cycle in all cases. This reflects the relatively low temperatures required for the production of this isotope by the CN-cycle.

(b) The ^{17}O profile is remarkable, showing a steep gradient in the central region. This is because ^{17}O is produced by the ON cycle which requires higher temperatures to become effective.

(c) The isotope ^{18}O is fragile and effectively destroyed by the $^{18}\text{O}(p,\alpha)^{15}\text{N}$ reaction.

These results are well known in the literature, but it is important to understand the surface abundances resulting after FDUP and SDUP for different stellar masses. The

efficiency of FDUP in modifying the surface abundances is related to the maximum penetration of the convective envelope on the RGB. In Fig. 4, the solid vertical line marks the convective boundary as determined by the Schwarzschild criterion and the dashed vertical line marks the position of the boundary when extra mixing beyond the formal convective boundary is considered (see Section 3.2.2 for details).

After FDUP, the change in the surface composition of a certain isotope depends on the shape of its profile inside the star. For example, the peak of the ^{13}C profile is located near the middle part of the star, so that envelope convection is able to smear out the profile, causing an increase in the ^{13}C surface abundance, or a decrease in the $^{12}\text{C}/^{13}\text{C}$ ratio. For the isotope ^{17}O , the situation is highly dependent on the stellar mass because the main production of ^{17}O is concentrated in the inner part. Fig. 4a which shows the case of a $1.4M_{\odot}$ as an example, illustrates that in low mass stars ($M \leq 2M_{\odot}$) envelope convection does not completely smear out the ^{17}O peak. This makes the ^{17}O profile sensitive to mixing in stars of $M \leq 2M_{\odot}$, so that any additional mixing below the envelope will increase its surface abundance. This effect is less pronounced in stars with $M \geq 3M_{\odot}$ (Fig. 4b shows the case of a $5M_{\odot}$ as an example in this mass range), where the ^{17}O bump is fully engulfed by the formal convective envelope, so extra mixing will not significantly alter its surface abundance in this mass range.

Table 3 summarizes the values of $^{16}\text{O}/^{17}\text{O}$, $^{12}\text{C}/^{13}\text{C}$ and $^{14}\text{N}/^{15}\text{N}$ after the FDUP and SDUP (if any, as we show later) in the case of standard convective mixing, together with those inferred from observations by Tsuji08 and other independent field star observations. The stars in the sample of Tsuji08 are advanced in evolution, but did not experience the third dredge up during the AGB phase. This is evident from the carbon surface abundances (Tsuji 2014, private communication). Thus, the comparison can be restricted to the effects of FDUP and SDUP only.

It is not easy to make a direct comparison between predicted surface abundances and observations, since this comparison is model-dependent on theoretical and observational grounds. Deriving the isotopic ratios observationally involves several sources of uncertainty like the dispersion in the ratios obtained from different lines, and inaccuracy in the atmospheric model parameters. Systematic errors may also be present, such as the uncertainty in the continuum position and departures from local thermodynamic equilibrium (LTE) (Abia et al. 2012), in addition to the difficulties that are inherent in the spectral analysis of very cool stars. The fact that atmospheric values are model-dependent causes discrepancies between observational results among different groups, and consequently, affect the subsequent discussion (Ramstedt & Olofsson 2014). On the other hand, theoretical models are also challenged by uncertainties in convective mixing, mass loss and nuclear reaction rates, where standard FDUP models often face difficulties in explaining carbon and oxygen surface abundances, particularly in low-mass stars. While being vigilant to these limitations, a careful comparison is useful for the sake of a better understanding.

Fig. 5 shows the $^{16}\text{O}/^{17}\text{O}$ ratios as a function of stellar mass, along with the theoretical predictions by Boothroyd & Sackmann (1999), Abia et al. (2012), Karakas & Lattanzio (2014) and the available observations. The predicted $^{16}\text{O}/^{17}\text{O}$ shows a distinct behavior between

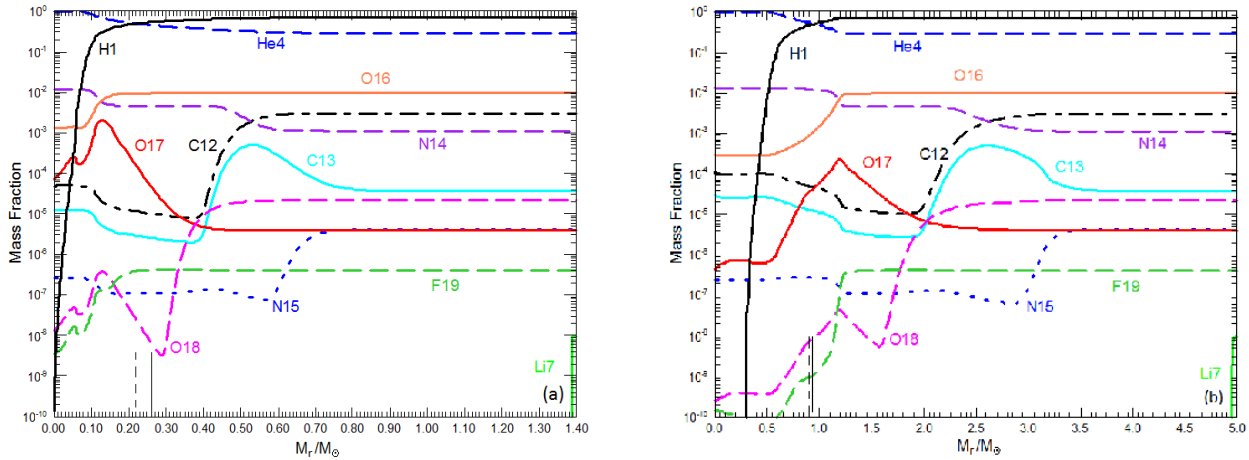


Figure 4. Abundance profiles of H, He and several CNO elements after core H-burning in the stellar masses (a) $1.4M_{\odot}$ and (b) $5M_{\odot}$. The solid lines mark the deepest penetration in mass of the convective envelope, while the dashed lines mark that when envelope overshooting is invoked. See text for details.

high and low mass stars, which will be discussed separately. For the higher masses ($M > 2M_{\odot}$), the standard calculation predicts $^{16}\text{O}/^{17}\text{O}$ ratios that fit the observed range within the error bars on the stellar masses. The relative spread in the observational values in this mass range cannot be explained by overshooting since in these stars the bump in the ^{17}O profile is fully mixed by the formal convective envelope as shown in Fig. 4b, so overshooting will not introduce a significant change to the standard predictions. Therefore, we attribute this spread to the uncertainties in describing the properties of the relatively cool red giants. This is a general feature of observationally inferred data due to the above mentioned uncertainties in measuring faint lines in their spectra which may result in considerably variant ratios for the same object among different observations. We expect that the error bars of these ratios are underestimated, particularly in stars like α Cet and α Her whose ratio varies considerably among different works as shown in Table 3.

In the case of the lower mass stars, the theoretical $^{16}\text{O}/^{17}\text{O}$ is higher than most data points obtained from observations. The results of standard calculation by other groups shown in the figure indicate a similar behavior. It is noted that the high observational $^{16}\text{O}/^{17}\text{O}$ values in the low mass stars like α Tau, ν Vir, σ Lib, β Peg, δ Vir, and RR UMi, which are denoted by up-pointing triangles in Fig. 5, are estimations due to the uncertainties in measuring faint lines like $^{12}\text{C}^{17}\text{O}$ in relatively cool atmospheres, where at such low temperatures the absorption lines are strong causing severe blending by several weak lines and introducing uncertainties (Tsuji08). Due to such complications, weak lines couldn't be measured at all for $^{12}\text{C}^{17}\text{O}$ in these stars, and $^{16}\text{O}/^{17}\text{O}$ is not well determined. Thus, these observational data points are not reliable to compare to our calculation. Our discussion is based on the low observational ratios in low mass stars which are more definitive, with well-determined error bars.

The overproduction of $^{16}\text{O}/^{17}\text{O}$ in low mass stars in our model shows that more ^{17}O needs to be mixed to the surface in order to lower the $^{16}\text{O}/^{17}\text{O}$ ratio. This may be achieved by

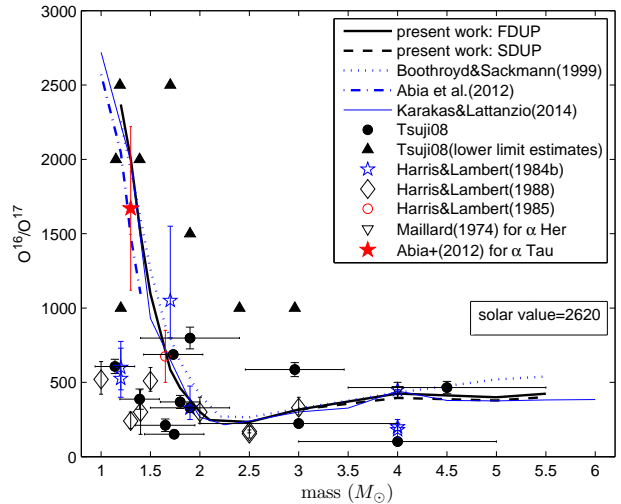


Figure 5. Calculated $^{16}\text{O}/^{17}\text{O}$ ratios for the 21 giants after FDUP (solid line) and SDUP (dashed line) versus stellar mass. Calculation by Boothroyd & Sackmann (1999), Abia et al. (2012) and Karakas & Lattanzio (2014) are also shown for comparison. Observations are indicated as data points. The errors on the masses are as listed in Table 2.

extra mixing or overshooting at the bottom of the convective envelope. In order to constrain this overshooting, a better understanding is required for the role of first and second dredge up for the whole range of masses under consideration.

It is known that after the star leaves the main sequence, FDUP alters significantly the surface abundances as it enriches the envelope with ^4He , ^{13}C , ^{17}O and ^{14}N and reduces its ^{12}C , ^{15}N and ^{18}O abundance. Every star that evolves to the AGB experiences the FDUP episode, and starts its early AGB phase with a sharp composition discontinuity at the point of maximum penetration of the FDUP. The H-burning shell in low-mass stars represents an entropy bar-

Table 3. M_{RGB} (in solar units) and the surface number abundances after FDUP and SDUP (if any, listed in parenthesis): *a*: surface abundances with standard mixing (present work), *b*: Tsuji08, *g*: Harris and Lambert (1984b), *h*: H85: Harris et al. (1985), *i*: Smith and Lambert (1990), *j*: Decin et al. (2003), *k*: Maillard (1974), *l*: Hinkle et al. (1976).

Object	M_{RGB}	$^{16}\text{O}/^{17}\text{O}^a$	$^{16}\text{O}/^{17}\text{O}^b$	$^{16}\text{O}/^{17}\text{O}$	$^{12}\text{C}/^{13}\text{C}^a$	$^{12}\text{C}/^{13}\text{C}^b$	$^{12}\text{C}/^{13}\text{C}$	$^{14}\text{N}/^{15}\text{N}^a$
δ Vir	1.19	2370	> 2500		32	12.3 ± 1.2	16 ± 4^i	551
α Tau	1.2	2370	> 1000	600_{+130}^{-150g}	30	10.6 ± 1.0	$10 \pm 2^{i,j}$	551
				525_{+250}^{-125g}			9 ± 1^g	
RRUMi	1.15	2006	> 2000		30	10.0 ± 0.8		598
RZ Ari	1.14	2006	607 ± 48		30	7.9 ± 0.8		598
δ Oph	1.39	1500	387 ± 68		29	11.1 ± 0.9		690
ν Vir	1.39	1500	> 2000		29	8.7 ± 1.3	12 ± 2^i	690
τ^4 Eri	1.73	461	687 ± 14		24	12.4 ± 0.3		963
10 Dra	1.74	461	151 ± 11		24	14.8 ± 1.6	12 ± 3^i	963
β Peg	1.7	462	> 2500	1050_{+500}^{-250g}	24	7.7 ± 0.5	8 ± 2^i	963
				$\geq 100^g$			5 ± 3^j	
30g Her	1.65	462	211 ± 42	$675_{-175}^{+175} h$	24	12.5 ± 1.1	10 ± 2^i	963
σ Lib	1.9	301	> 1500		22	7.5 ± 0.3		1126
R Lyr	1.8	301	368 ± 44		22	6.4 ± 0.3		1126
μ Gem	1.9	301	798 ± 73	$325_{+150}^{-75} g$	22	10.5 ± 1.2	13 ± 2^i	1126
				$\geq 100^g$				
OP Her	1.9	246	329 ± 31		22	11.3 ± 1.2		1103
ρ Per	2.4	234	> 1000		22	9.7 ± 1.0	15 ± 2^i	1307
α Cet	2.96	318(317)	586 ± 47		21(21)	11.1 ± 0.8	10 ± 2^j	1460(1501)
λ Aqr	2.96	318(317)	> 1000		21(21)	7.9 ± 1.4		1460(1501)
XY Lyr	3.0	424(395)	223 ± 16		21(20)	15 ± 0.4		1528(1610)
δ^2 Lyr	4.5	400(378)	465 ± 41		21(20)	16.2 ± 1.5		1503(1629)
α Her	4.0	424(402)	102 ± 8	180_{+70}^{-50g}	21(20)	11.1 ± 0.7	$17 \pm 4^{g,l}$	1538/1642
				200_{+25}^{-25g}				
				$\approx 450^g$				
				450_{+50}^{-50k}				
BS 6861	5.35	424(402)	> 1000		21(20)	48.5 ± 2.9		1538(1642)
Initial		2620			90			270

rier that prevents any deeper penetration of the convective envelope, and thus no further change in the surface abundances takes place. However, for solar metallicity stars of masses above $3\text{--}4M_{\odot}$, the gravitational energy release due to the contracting core and the increased energy flux from the burning He-shell lead to an expansion so that the H-shell is pushed outwards in mass to low temperatures causing a temporary extinction in the H-burning shell. This situation, coupled to the drop in the temperature of the expanding layers and the increase in the opacity (Iben & Renzini 1983), causes convection to deepen in a second dredge up (SDUP)

event and mixes out the composition discontinuity left over by the FDUP. Therefore, SDUP introduces further changes in the surface abundances of stars of masses $\gtrsim 4M_{\odot}$.

Fig. 6 shows the maximum penetration of the convective envelope at FDUP and SDUP as a function of the initial stellar mass. It is clear from the figure that for $M < (4\text{--}5)M_{\odot}$, SDUP doesn't penetrate deeper than the FDUP, and thus, it does not introduce significant change to the surface composition. This is in agreement with Karakas & Lattanzio (2014), for their solar metallicity case. Their Fig. 7 exhibits similar general features and also indicates a deepest penetration of

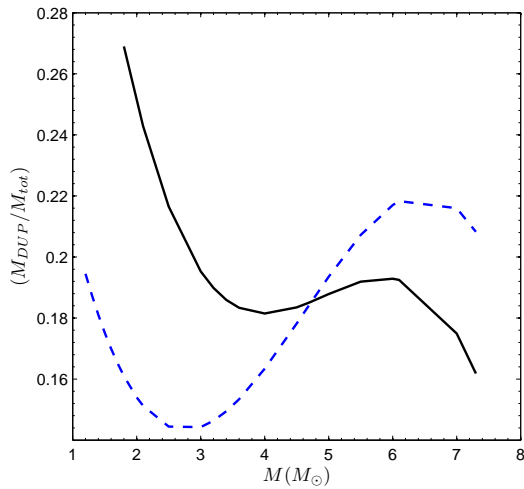


Figure 6. Fractional mass reached by the convective envelope at FDUP (dashed line) and SDUP (solid line). SDUP is deeper than FDUP only in models of stellar masses $\geq 5M_{\odot}$. The mass on the y-axis is given as the mass reached by the dredge up over the total initial stellar mass, in solar units.

FDUP in $\approx 2.5M_{\odot}$ stars. For stars of $M > 6M_{\odot}$, the expansion is strong and convection extends deeper inwards. Since low mass stars do not experience SDUP, this implies that their observed surface abundances on the AGB phase are actually “inherited” from the RGB phase. Therefore, one way to account for the discrepancy between calculated and observationally inferred values of $^{16}\text{O}/^{17}\text{O}$ in these stars is to invoke extra mixing below the convective envelope on the RGB phase.

3.2.2 Predictions of surface abundances with extra mixing

Overshooting is applied as outlined in Section 2.1 and we find that $f = 0.125$ provides the best estimation for its efficiency in low mass stars. Fig. 7 shows the $^{16}\text{O}/^{17}\text{O}$ ratios of our star sample in the standard case and with overshooting. The low observational $^{16}\text{O}/^{17}\text{O}$ in low mass stars can now be fitted quite well within the error bars on the stellar masses. It is noted how overshooting has a minor effect in stars of $M \geq 3M_{\odot}$. This is expected due to the shape of the ^{17}O abundance profile in these stars as discussed earlier in connection with the shape of the ^{17}O profile in these stars. The calculated and observationally inferred values for these stars are generally in a good agreement.

Fig. 8 shows the predicted carbon and nitrogen abundances in the standard case and with overshooting. Observations are also shown for comparison. A well-known problem arises in explaining the surface carbon abundances in stars of $M \leq 2M_{\odot}$, where our extra mixing treatment cannot explain the low carbon observed in these giants. Calculations using standard mixing by Boothroyd & Sackmann (1999) and Karakas & Lattanzio (2014) show a similar problem. A different non-standard mixing process seems to be required in low-mass stars ($< 2M_{\odot}$) which can reduce the abundance of ^{12}C by mixing it to the hotter regions of the H-burning shell, allowing for some nuclear processing. Such mixing pro-

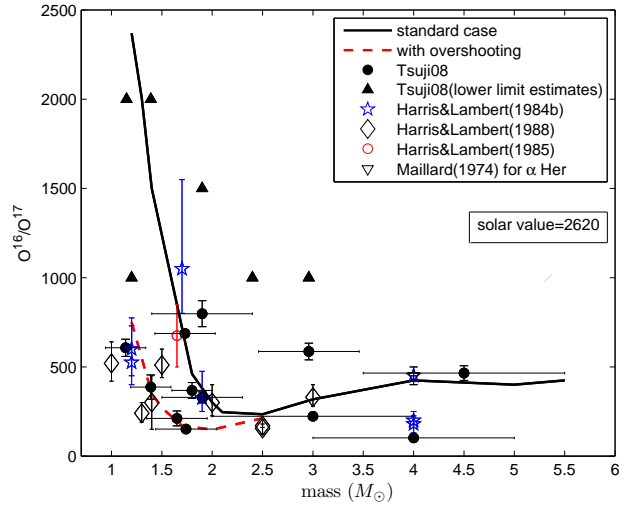


Figure 7. The $^{16}\text{O}/^{17}\text{O}$ ratios obtained in the standard case and in the case of envelope overshooting with $f=0.125$. Several observations are shown for comparison.

cess is linked to the long evolutionary time of the low-mass stars while ascending the RGB. As discussed in some details in Karakas & Lattanzio (2014), the so-called “thermohaline mixing” or “salt-finger instability” seems to be one possible description of this extra mixing in low-mass red giant stars. This is still an unsettled problem in stellar modeling. Nitrogen abundances, on the other hand, show a scatter in the observed data. This will be discussed in connection with the $^{14}\text{N}/^{15}\text{N}$ ratios in Section 3.3.2. In general, Fig. 8b shows that the observations pose no serious contradiction with the values predicted by the stellar models which, on average, reasonably reproduce the observationally inferred data.

3.3 Effect of modified nuclear reaction rates

3.3.1 The $^{16}\text{O}/^{17}\text{O}$ ratio

In order to investigate the effect of the ^{17}O production and destruction reaction rates on the $^{16}\text{O}/^{17}\text{O}$ ratios, four different evaluations of the proton-capture reactions $^{16}\text{O}(p,\gamma)^{17}\text{F}$, $^{17}\text{O}(p,\gamma)^{18}\text{F}$ and $^{17}\text{O}(p,\alpha)^{14}\text{N}$ are used. In particular, we use the compilations by Sergi et al. (2014) (SE14), Sallaska et al. (2013) (SA13), Iliadis et al. (2010) (IL10) and Chafa et al. (2007) (CH07). The $^{16}\text{O}/^{17}\text{O}$ ratios obtained are shown in Fig. 9 for both cases: standard mixing (Fig. 9a) and envelope overshooting with $f = 0.125$ (Fig. 9b). The four sets of rates give very similar $^{16}\text{O}/^{17}\text{O}$ values in the considered mass range. None provides a reasonable agreement between model predictions and observations unless overshooting is included. This consistency shows that the existing discrepancy cannot be removed without invoking deeper mixing. Fig. 9b shows a better fit of the observed data within the error bars in the low mass stars.

The effect of the reaction rates uncertainties is also worth exploring. Since the SA13 compilation is based on a Monte Carlo simulation and the rates have statistically well-defined uncertainties (Longland et al. 2010; Longland

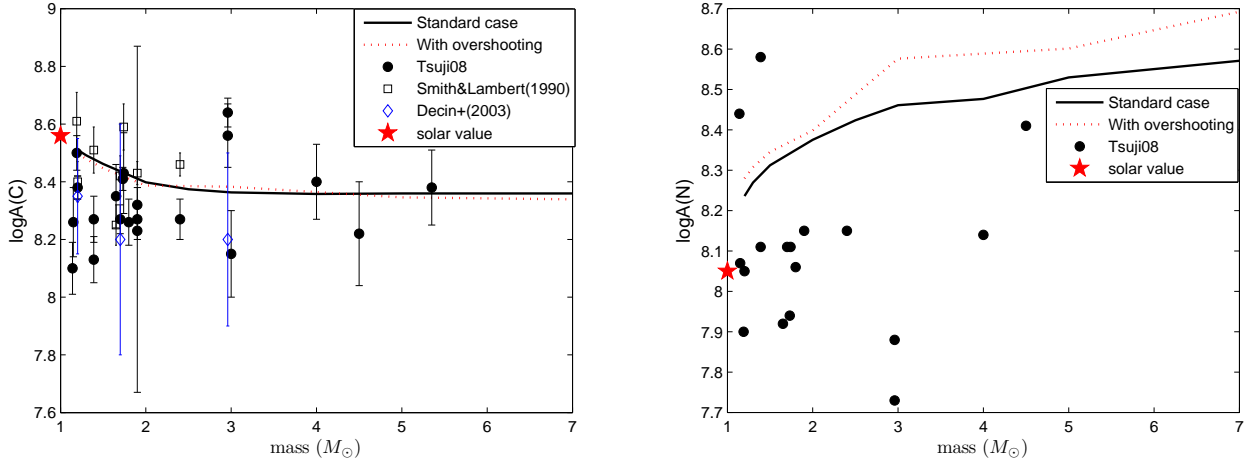


Figure 8. The predicted surface abundances of (a) carbon and (b) nitrogen with observations as shown. The initial solar values of carbon and nitrogen are 8.5601 and 8.0499, respectively and are indicated by a star symbol.

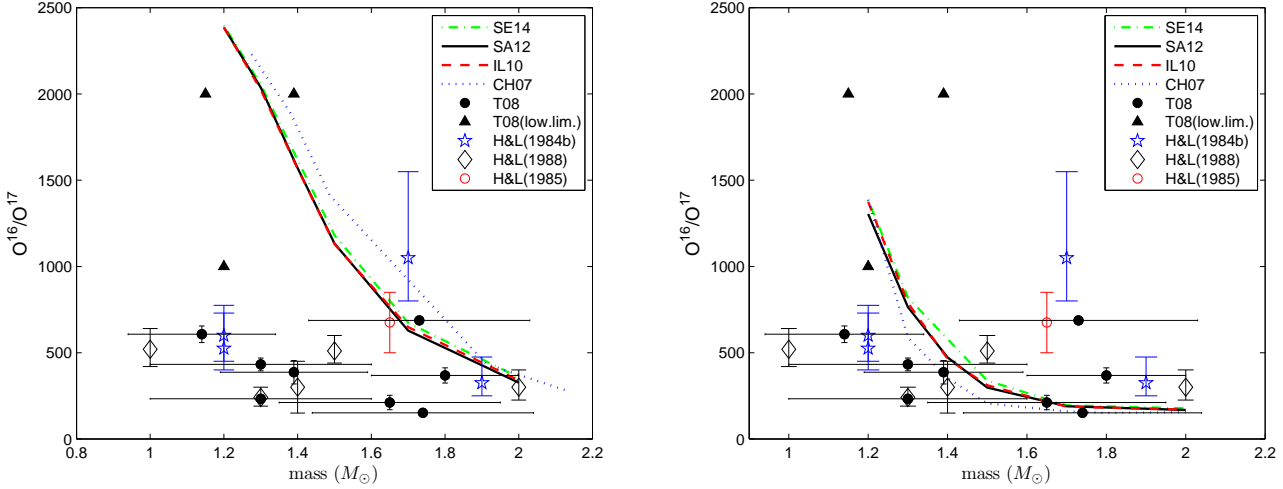


Figure 9. The $^{16}\text{O}/^{17}\text{O}$ ratios calculated for the 21 giants, with four different sets of compilations of relevant reaction rates (see text for details). Left panel shows the case with standard mixing and the right panel is that with overshooting ($f = 0.125$). Observational data are also included.

2012; Iliadis et al. 2014), the $^{16}\text{O}/^{17}\text{O}$ ratios are calculated using the recommended, high and low rates, where the rate boundaries correspond to a 95% coverage probability. The rates uncertainty has a very minor effect on the tracks during H-shell burning but none along the RGB, and hence it does not affect our mass determination. However, the $^{16}\text{O}/^{17}\text{O}$ ratios show a larger sensitivity to these uncertainties, as shown in Fig. 10. It is found that the observational data can be better explained when the whole range of uncertainty on the involved reaction rates is considered since the discrepancy between predictions and observations becomes less pronounced. On the other hand, the $^{12}\text{C}/^{13}\text{C}$ ratios are found to be immune to the uncertainties on the considered rates. The difference in $^{12}\text{C}/^{13}\text{C}$ obtained with the high rates and low rates does not exceed 3%.

3.3.2 The $^{14}\text{N}/^{15}\text{N}$ ratio

The surface $^{14}\text{N}/^{15}\text{N}$ ratio is worth considering in connection with the latest evaluation of the $^{14}\text{N}(p, \gamma)^{15}\text{O}$ rate (Marta et al. 2011). This ratio is calculated for the mass range under consideration after FDUP and SDUP. It is found that our values are higher by $\sim 20\%$ relative to those by El Eid (1994) in stars of masses $\geq 3M_{\odot}$. This is expected and due to the NACRE $^{14}\text{N}(p, \gamma)^{15}\text{O}$ rate (Angulo et al. 1999) used in that work, which is almost a factor of 2 higher than the revised rate at stellar temperatures (see Halabi, El Eid & Champagne (2012) for the expression of this rate and explicit discussion). However, our $^{14}\text{N}/^{15}\text{N}$ is about 12% lower in the low-mass stars.

It is quite unfeasible to verify our findings since $^{14}\text{N}/^{15}\text{N}$ ratios are difficult to measure in RGB stars from CN lines because they are too weak even in very high resolution spectra. In fact, the $^{14}\text{N}/^{15}\text{N}$ ratio is difficult to measure di-

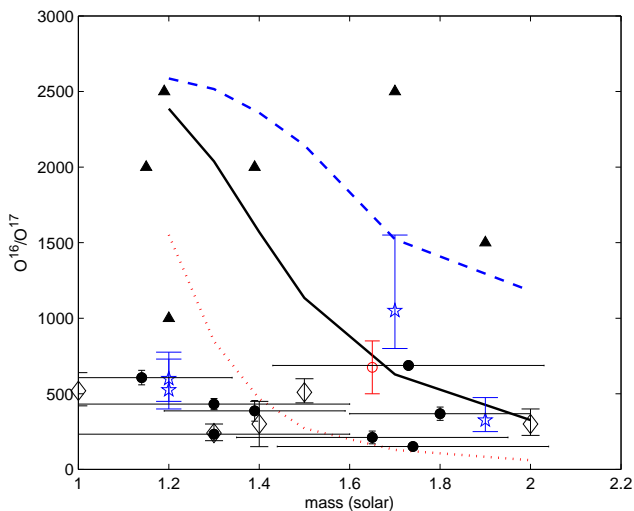


Figure 10. The SA13 set of rates in the standard case. Shown are the results with the recommended set of rates (solid line), the high rates (dotted) and low rates (dashed). Observational data are the same as in Fig. 9.

rectly for molecules containing carbon (Roueff et al. 2015). On the other hand, stars in the early AGB phase are O-rich and then their spectra would be dominated by oxide molecules and not by C-bearing molecules. Oxide molecules like NO cannot be observed in the visual or near-IR region in these stars (Carlos Abia, private communication). Observations in radio-wavelengths can in principle detect some N-bearing molecules from which $^{14}\text{N}/^{15}\text{N}$ may be derived, but in this case one would probably be looking at the circumstellar envelope of the star not the photosphere. Circumstellar N ratios might be affected by the incoming UV radiation from the ISM triggering non-kinetic equilibrium chemistry and thus, might not represent the stellar photospheric ratios (Hedrosa et al. 2012). Theoretical predictions of the $^{14}\text{N}/^{15}\text{N}$ ratios, particularly the changes induced by the revision of the $^{14}\text{N}(p, \gamma)^{15}\text{O}$ reaction rate may benefit from future observations or one may resort to the chemical analysis of pre-solar grains originating from the envelopes of late AGB stars.

4 CONCLUSIONS

A sample of observed RGB and early AGB stars was considered and their masses were obtained using extended evolutionary tracks. This was done without the need of extrapolating the evolutionary tracks at lower effective temperatures as it has been done in the work by Tsuji08. The present evolutionary tracks include the effect of mass-loss, which becomes important during the red giant phases, especially for the higher stellar masses under consideration. This investigation includes an analysis of the physical conditions in the overshooting region and the effect of this overshooting on the abundance yields. We find that overshooting is needed to reconcile observational oxygen abundances with model predictions particularly in low mass red giants. Although

Tsuji08 has interpreted the discrepancies between the predicted and observational abundances as an effect of extra mixing, he did not provide models including this extra mixing to see how the discrepancies may be understood. We showed that extra mixing based on the mixing of chemical elements by diffusion explains reasonably the observationally inferred oxygen isotopic ratios. It is important to realize the challenges facing such observations and the uncertainties involved in the available data. In this regard, the spread in the observational data in the low and high mass ranges was discussed in connection with the inherent difficulties in analyzing the spectra of these relatively cool stars and the uncertainties involved in measuring faint lines like $^{12}\text{C}^{16}\text{O}$. Our overshooting treatment cannot, however, explain the low surface carbon abundances in low mass stars. Another mixing mechanism seems to be required during the long evolutionary time needed for the low-mass stars to ascend the red giant branch.

Furthermore, the present calculations were carried out using recent determinations of proton-capture rates which have reliable statistical error bars. This allows us to draw conclusions on the uncertainties involving CNO surface abundances. In particular, the effect of recent evaluations of the reaction rates on the production and destruction of ^{17}O was explored. The experimentally suggested uncertainty of these rates provides a better fit of the $^{16}\text{O}/^{17}\text{O}$ observed in low mass stars yet does not exclude the need to invoke overshooting. Additional mixing beyond the convective envelope as determined by the Schwarzschild criterion is found to be necessary to better explain the observational $^{16}\text{O}/^{17}\text{O}$ surface abundances, especially in low mass stars. Moreover, the effect of $^{14}\text{N}(p, \gamma)^{15}\text{O}$ rate on the $^{14}\text{N}/^{15}\text{N}$ ratios was studied in the considered mass range.

As a final remark, our approach in the present study was to consider a sample of red giant stars to see how far standard calculation predictions agree with observations. A comprehensive comparison between stellar models and observations based on the analysis of the effect of extra mixing was presented and linked to the uncertainties in key nuclear reaction rates affecting the CNO abundances in red giants. Comparing theoretical predictions of stellar models to available observations is required in order to constrain parametrized approaches in determining the efficiency and extension of mixing at convective boundaries. Future multi-dimensional simulations of convection may introduce an improved local description of this mixing and provide insight towards a better understanding of the physical processes involved.

This work was supported by the Lebanese National Council for Scientific Research (CNRS) under grant award number 11179-102899. The authors wish to thank Christian Illiadis and Richard Longman for providing the nuclear reaction rates and for their valuable input and discussions on the manuscript. The authors also acknowledge the anonymous referee for the constructive comments and suggestions that helped improve the quality of this work.

REFERENCES

- Abia, C., Palmerini, S., Busso, M., & Cristallo, S. 2012, *A&A*, 548, A55

- Angulo, C., Arnould, M., Rayet, M., et al. 1999, *Nucl. Phys. A*, 656, 3A
- Baschek, B., Scholz, M., & Wehrse, R. 1991, *A&A*, 246, 374
- Bildsten, L., Paxton, B., Moore, K., Macias, P. J. 2012, *ApJ*, 744L, 6B
- Blackwell, D. E., Petford, A. D., & Shallis, M. J. 1980, *A&A*, 82, 249
- Boothroyd, A. I. & Sackmann, I.-J. 1999, *ApJ*, 510, 232
- Bowen, G. H., 1988, *ASSL*, 148, 3B
- Busso, M., Trippella, O., Maiorca, E., Palmerini, S. 2014, *AIPC*, 1595, 41B
- Caughlan, G. R., & Fowler, W. A. 1988, *Atomic Data and Nucl. Data Tables*, 40, 283
- Chafa, A. et al., 2007, *PRC* 75, 035810
- Charbonnel, C. 1994, *A&A* 282, 811
- Charbonnel, C., & Do Nascimento, J. D. 1998, *A&A*, 336, 915
- Claret, A. 2004, *A&A*, 424, 919
- Cyburt et al. 2010, *ApJS* 189, 240
- Decin, L., Cohen, M., Eriksson, K., Gustafsson, B., Huygen, E., Morris, P., Plez, B., Sauval, J., Vandenbussche, B., Waelkens, C. 1997, *ESASP*, 419, 185D
- Decin, L., Vandenbussche, B., Waelkens, C., et al. 2003, *A&A*, 400, 709
- Denissenkov, P., VandenBerg, D., Hartwick, D., Herwig, F., Weiss, A., Paxton, B. 2015, *MNRAS*, 448, 3314
- El Eid, M. F. 1994, *A&A*, 285, 915
- El Eid, M. F., The, L.-S., & Meyer, B. 2009, *Space Sci. Rev.*, 147, 1
- Freytag, R., Ludwig, H., & Steffen, M. 1996, *A&A*, 313, 497
- Gilroy, K. K. & Brown, J. A. 1991, *ApJ* 371, 578
- Gratton, R. G., Sneden, C., Carretta, E., & Bragaglia, A. 2000, *A&A*, 354, 169
- Halabi, G. M., El Eid, M., Champagne, A., 2012, *ApJ*, 761, 10
- Harris, M. J., Lambert, D. L. & Smith, V.V. 1988, *ApJ*, 325, 768
- Harris, M. J. & Lambert, D. L., 1984a, *ApJ* 281, 739
- Harris, M. J. & Lambert, D. L., 1984b, *ApJ* 285, 674
- Harris, M. J., Lambert, D. L. & Smith, V. V. 1985, *ApJ*, 299, 375
- Hedrosa, R. P., Abia, C., Plez, B., & Domínguez, I. 2012, *PoS(NIC XII)006*
- Iben, I., Jr., Renzini, A., 1983, *Ann. rev. Astron. Astrophys.* 21, 271
- Iliadis, C., Longland, R., Champagne, A., Coc, A. 2010, *Nucl.Phys. A* 841, 251-322
- Iliadis, C., Longland, R., Coc, A., Timmes, F., X., Champagne, A. 2014, *J. Phys. G: Nucl. Part. Phys.*, 42, 034007
- Karakas, A. & Lattanzio J. 2014, *arXiv:1405.0062*
- Kippenhahn, R., & Weigert, A. 1990, *Stellar Structure and Evolution* (Berlin: Springer-Verlag)
- La Cognata, M. et al. 2010, *APJ*, 708, 796
- Lambert, D. L., Gustafsson, B., Eriksson, K., Hinkle, K. H. 1986, *ApJ Suppl.* 62, 373
- Lambert, D. L. & Ries L. M. 1981, *ApJ* 248, 228
- Langer, N., El Eid, M. F., & Fricke, K. J. 1985, *A&A*, 145, 179
- Lebzelter, T., Nowotny, W., Höfner, S., Lederer, M. T., Hinkle, K. H., & Aringer, B. 2010, *A&A* 517, A6
- Longland, R., Iliadis, C., Champagne, A., Newton, J., Ugalde, C., Cocc, A., Fitzgerald, R. 2010, *Nucl. Phys. A*, 841, 1
- Logland, R. 2012, *A&A*, 548A, 30L
- Luck, R. E. 1994, *ApJS*, 91, 309
- Maillard, J. P. 1974, *Highlights Astron.*, 3, 269
- Marta et al. 2011, *Phys. Rev. C*, 83, 045804
- Mocák, M., Campbell, S. W., Müller, E., Kifonidis, K. 2010, *A&A*, 520, 114
- Palmerini, S., La Cognata, M., Cristallo, S., & Busso, M. 2011, *ApJ*, 729, 3
- Palmerini, S., Sergi, M. L., La Cognata, M., Lamia, L., Pizzone, R. G., Spitaleri, C. 2013, *ApJ*, 764, 128P
- Piau, L., Kervella, P., Dib, S. & Hauschildt P. 2011, *A&A* 526, A100
- Pilachowski, C., Sneden, C., Freeland, E., & Casperson, J. 2003, *AJ*, 125, 794
- Ramstedt, S. & Olofsson, H. 2014, *A&A*, 566A, 145R
- Recio-Blanco, A., & de Laverny, P. 2007, *A&A*, 461, L13
- Reimers, D. 1975, *Mem. Soc. R. Sci Liege*, 8, 369
- Roueff, E., Loison, J. C. & Hickson, K. M. 2015, *A&A* 576, A99
- Sallaska, A. L., Iliadis, C., Champagne, A. E., Goriely, S., Starrfield, S., Timmes, F. X. 2013, *ApJS* 207, 18
- Sergi, L. et al. 2014, *AIPC*, 1594, 201S
- Shetrone, M. D. 2003, *ApJ*, 585, L45
- Smith, V. V. & Lambert D. L., 1985, *ApJ*, 294, 326
- Smith, V. V., & Lambert, D. L. 1990, *ApJS*, 72, 387
- Tautvaišienė, G., Edvardsson, B., Tuominen, I., & Ilyin, I. 2000, *A&A*, 360, 499
- Tautvaišienė, G., Edvardsson, B., Puzeras, E., & Ilyin, I. 2005, *A&A*, 431, 933
- Tautvaišienė, G., Edvardsson, B., Puzeras, E., Barisevičius, G. & Ilyin, I. 2010, *Mon. Not. R. Astron. Soc.* 409, 1213
- Tsuji, T. 1991, *A&A*, 245, 203
- Tsuji, T. 2008, *A&A* 489, 1271
- Vassiliadis, E., & Wood, P. R., 1992, *Proc. ASA*, 10, 1
- Woo, J. H. & Demarque, P. 2001, *AJ*, 122, 1602W